# Precision Modeling of JWST's First Cluster Lens SMACS J0723.3–7327[*]

Guillaume Mahler[1,2] , Mathilde Jauzac[1,2,3,4] , Johan Richard[5] , Benjamin Beauchesne[6,7] , Harald Ebeling[8] ,
David Lagattuta[1,2] , Priyamvada Natarajan[9,10,11] , Keren Sharon[12] , Hakim Atek[13] , Adélaïde Claeyssens[14] ,
Benjamin Clément[6] , Dominique Eckert[15] , Alastair Edge[1] , Jean-Paul Kneib[6] , and Anna Niemiec[1,2]

[1] Centre for Extragalactic Astronomy, Durham University, South Road, Durham, DH1 3LE, UK; guillaume.mahler@durham.ac.uk
[2] Institute for Computational Cosmology, Durham University, South Road, Durham, DH1 3LE, UK
[3] Astrophysics Research Centre, University of KwaZulu-Natal, Westville Campus, Durban 4041, South Africa
[4] School of Mathematics, Statistics & Computer Science, University of KwaZulu-Natal, Westville Campus, Durban 4041, South Africa
[5] Univ Lyon, Univ Lyon1, Ens de Lyon, CNRS, Centre de Recherche Astrophysique de Lyon UMR5574, F-69230, Saint-Genis-Laval, France
[6] Institute of Physics, Laboratory of Astrophysics, École Polytechnique Fédérale de Lausanne (EPFL), Observatoire de Sauverny, CH-1290 Versoix, Switzerland
[7] European Southern Observatory, Alonso de Cordova 3107, Vitacura, Santiago, Chile
[8] Institute for Astronomy, University of Hawaii, 640 N Aohoku Pl, Hilo, HI 96720, USA
[9] Department of Astronomy, Yale University, 52 Hillhouse Avenue, New Haven, CT 06520, USA
[10] Department of Physics, Yale University, P.O. Box 208121, New Haven, CT 06520, USA
[11] Black Hole Initiative, Harvard University, 20 Garden Street, Cambridge, MA 02138, USA
[12] Department of Astronomy, University of Michigan, 1085 S. University Ave, Ann Arbor, MI 48109, USA
[13] Institut d'astrophysique de Paris, CNRS, Sorbonne Université, 98bis Boulevrad Arago, F-75014, Paris, France
[14] The Oskar Klein Centre, Department of Astronomy, Stockholm University, AlbaNova, SE-10691 Stockholm, Sweden
[15] Department of Astronomy, University of Geneva, ch. d'Ecogia 16, CH-1290 Versoix, Switzerland

## Abstract

Exploiting the fundamentally achromatic nature of gravitational lensing, we present a lens model for the massive galaxy cluster SMACS J0723.3−7323 (SMACS J0723; $z = 0.388$) that significantly improves upon earlier work. Building on strong-lensing constraints identified in prior Hubble Space Telescope (HST) observations, the mass model utilizes 21 multiple-image systems, 17 of which were newly discovered in Early Release Observation data from the JWST. The resulting lens model maps the cluster mass distribution to an rms spatial precision of $0''32$, and is publicly available. Consistent with previous analyses, our study shows SMACS J0723.3 to be well described by a single large-scale component centered on the location of the brightest cluster galaxy. However, satisfying all lensing constraints provided by the JWST data, the model points to the need for the inclusion of an additional, diffuse component west of the cluster. A comparison of the galaxy, mass, and gas distributions in the core of SMACS J0723 based on HST, JWST, and Chandra data reveals a concentrated regular elliptical profile along with tell-tale signs of a recent merger, possibly proceeding almost along our line of sight. The exquisite sensitivity of JWST's NIRCam reveals in spectacular fashion both the extended intracluster light distribution and numerous star-forming clumps in magnified background galaxies. The high-precision lens model derived here for SMACS J0723 demonstrates the unprecedented power of combining HST and JWST data for studies of structure formation and evolution in the distant universe.

Unified Astronomy Thesaurus concepts: Galaxy clusters (584); Strong gravitational lensing (1643)

## 1. Introduction

Clusters of galaxies grow and evolve through large-scale merging processes and offer many valuable observables for astrophysical and cosmological studies of our universe. In statistically representative samples, clusters uniquely constrain key parameters of complex physical processes, such as structure formation, but also the cosmological parameters characterizing the underlying world model (Jullo et al. 2010; Acebron et al. 2017; Caminha et al. 2017; Schwinn et al. 2017). By measuring the mass distribution within clusters, we also gain insight into cluster-

specific properties such as their dark-matter content, the detailed spatial distribution and clustering of dark matter, and the cluster's merger geometry and history (e.g., Bradač et al 2008; Umetsu et al. 2009; Kneib & Natarajan 2011; Ebeling et al. 2017). Furthermore, potential offsets between the location of baryonic and dark matter profiles have been used to probe the nature of dark matter (e.g., its self-interaction cross-section; Markevitch et al. 2004; Randall et al. 2008; Wittman et al. 2018; Harvey et al. 2019).

Strong gravitational lensing provides an observational measure of the total enclosed mass of a cluster at a given radius and thus offers a powerful tool for studying both their dark and luminous matter content. Lensing occurs when the presence and concentration of mass generates a large enough curvature in spacetime near the cluster center to make different light paths from the same distant source converge within the field of view of the observer. Since the first spectroscopic confirmation of a giant gravitational arc in A370 (Soucail et al. 1987), strong gravitational lensing has evolved into a valuable and powerful technique for measuring the total mass of clusters over a wide range of evolutionary states and redshifts (e.g., Limousin et al. 2007; Richard et al. 2011; Sharon et al. 2015).

By refining the mass model of a lensing cluster through the identification of strong-lensing features, it is possible to quantify the magnifying power of the cluster for background sources at a given redshift, thereby calibrating galaxy clusters as cosmic telescopes for studies of the high-redshift universe (e.g., Mahler et al. 2019; Fox et al. 2022). The correct identification of multiply imaged background sources is crucial in this context, because these are the principal constraining features that permit us to precisely map the mass distribution in the cluster core. The high angular resolution of the Hubble Space Telescope (HST) has proven invaluable for such work, as determination of the source morphology is instrumental to the task of properly matching multiple lensed images of the same source.

The most ambitious example of this quest to date was the Hubble Frontiers Field Initiative (HFF; Lotz et al. 2017), which provided very deep HST observations ($\sim$180 orbits per target) in seven optical and near-IR (NIR) passbands. The HFF observed six massive clusters ($M \approx 10^{15} \ M_\odot$) at $z = 0.3$–0.6, selected for their lensing power and, specifically, their capability to strongly magnify very distant ($z > 6$) galaxies. The resulting deep images revealed a remarkable collection of hundreds of multiple images that provided unprecedented insights into the detailed mass distribution of clusters and, given their visual power, were showcased in numerous publications (e.g., Jauzac et al. 2014, 2016; Grillo et al. 2015; Sharon & Johnson 2015; Diego et al. 2016a, 2016b; Caminha et al. 2017; Mahler et al. 2018; Vanzella et al. 2021).

Providing an order-of-magnitude improvement in sensitivity, the JWST represents another dramatic leap forward in our efforts to probe the distant universe to ever larger depth, exploiting gravitational lensing. The enormous promise of JWST is exemplified in the release of JWST's first deep cluster observation, of SMACS J0723.3$-$7327 (hereafter, SMACS J0723), the results from which are discussed and presented in this paper.

Our paper is structured as follows. After a brief introduction of the target and the history of its discovery in Section 2, we summarize the most relevant ground- and space-based observations of SMACS J0723 in Section 3. Section 4 provides an overview of the analysis and modeling techniques used here, and Section 5 describes the results obtained from the analysis of JWST data in combination with prior HST data. We present a summary of our findings and conclusions in Section 6.

For the underlying cosmological model, we assume a Lambda cold-dark-matter ($\Lambda$CDM) concordance cosmology ($\Omega_\Lambda = 0.7$, $\Omega_m = 0.3$) and $h = 0.7$ throughout. In this cosmology, $1''$ corresponds to 5.3 kpc at the cluster redshift of $z = 0.3877$.

## 2. SMACS J0723.3$-$7323

SMACS J0723 was discovered in the course of the southern extension of the Massive Cluster Survey (MACS; Ebeling et al. 2001) and is included in the partial release of the MACS sample by Repp & Ebeling (2018).

The system's initial identification as a putative distant cluster was based on the presence of an unidentified X-ray source, 1RXS J072319.7$-$732735, with 64 detected photons in a 531 s exposure accumulated during the ROSAT All-Sky Survey (RASS; Voges et al. 1999). The source's high X-ray hardness ratio of 0.95 (HR1 in RASS parlance), very high even at the relatively high neutral-hydrogen density of more than $10^{21} \ \mathrm{cm}^{-2}$ at the source's low Galactic latitude ($b = -23$

deg), its high likelihood of being extended, as well as the absence of alternative plausible optical counterparts in shallow, archival Digital Sky Survey images, rendered 1RXS J072319.7 $-$732735 a prime candidate for follow-up observations. Consequently, SMACS J0723 was targeted in imaging and low-resolution spectroscopy observations with the 3.5 m New Technology Telescope at the European Southern Observatory (ESO) in 2002 and 2003, respectively, which unambiguously confirmed the system as a massive cluster and established its tentative redshift as $z = 0.404$ (see Section 5.1 for an improved redshift measurement).

## 3. Observations and Data Reduction

### 3.1. Optical and Near-IR Imaging

#### 3.1.1. James Webb Space Telescope

SMACS J0723 was observed in early 2022 June with several instruments on board JWST as part of the observatory's Early Release Observations (EROs).[16] Specifically, deep imaging was performed in the NIRCam filters F090W, F150W, F200W, F277W, F356W, and F444W (Figures 1 and 2). The central field was also imaged with Mid-Infrared Instrument (MIRI) and Near InfraRed Imager and Slitless Spectrograph (NIRISS).

Our analysis combines pre-JWST observations (described below) with NIRCam data and NIRSpec spectroscopy.

#### 3.1.2. Hubble Space Telescope

SMACS J0723 has been observed several times with multiple instruments on board the HST: first with the Wide-Field and Planetary Camera 2 (WFPC2) in the optical regime (F606W and F814W filters) in 2008 (GO-11103; PI: Ebeling); then in the same two filters, with the Advanced Camera for Surveys (ACS) in 2011 and 2014 for GO-12166 and GO-12884, respectively (both PI: Ebeling); and, finally, in 2017 with the Wide-Field Camera 3 (WFC3) and ACS in the F453W, F606W, F814W, F105W, F125W, F140W, and F160W passbands for the RELICS program (GO-14096; PI: Coe). In all cases, the observing time ranged from about a half orbit to one orbit per filter. Additional snapshot images in the F606W and F105W passbands were obtained with WFC3 in 2022 for GO-16729 (PI: Kelly).

### 3.2. Spectroscopy

#### 3.2.1. ESO

Shallow ($3 \times 970$ s) observations of the cluster were performed in 2019 March in moderate seeing conditions ($0''.72$) for Programme 0102.A-0718(A) (PI: Edge) with the Multi-Unit Spectroscopic Explorer (MUSE) integral field spectrograph on the ESO Very Large Telescope. The observation covered a $1 \times 1 \ \mathrm{arcmin}^2$ region centered on the brightest cluster galaxy (BCG) of SMACS J0723 and yielded spectra in the range from 480 to 930 nm of both lensing features and foreground/cluster galaxies.

The reduction of the MUSE data cube was performed using the official ESO pipeline (Weilbacher et al. 2020), with a number of specific improvements regarding self-calibration and sky subtraction specific to the crowded fields of lensing clusters. These are extensively discussed in previously

---

[16] https://www.stsci.edu/jwst/science-execution/approved-programs/webb-first-image-observations

**Figure 1.** JWST/NIRCam image of a $2 \times 2$ arcmin$^2$ area centered on the brightest cluster galaxy (BCG) of SMACS J0723. The overlaid white contours show the X-ray surface brightness (adaptively smoothed to $3\sigma$ significance using the algorithm of Ebeling et al. 2006) as observed with Chandra. Contours are spaced logarithmically by factors of 1.5, starting at three times the background level. The astrometric alignment of the two underlying images is accurate to about $1''$.

published work by Lagattuta et al. (2022) and Richard et al. (2021).

### 3.2.2. JWST

As part of the JWST's ERO of SMACS J0723, the observatory also acquired spectroscopic data with the Micro Shutter Array (MSA) NIRSpec of 58 individual galaxies, as well as spectra of all objects in the entire field with NIRISS in wide-field slitless mode. The total on-source exposure time ranged from 1.5 to 5 hr. Our first analysis presented here uses primarily NIRSpec MSA data (reduced two-dimensional spectra and one-dimensional extracted spectra of various multiple images) directly available from the ERO data release.

### 3.3. X-Ray Imaging Spectroscopy

SMACS J0723 was observed with the Advanced CCD Imaging Spectrometer (ACIS-I) on board the Chandra X-ray Observatory on 2014 April 14. The observations (Sequence Number 801329; ObsID 15296; PI: Murray) were performed in VFAINT mode for a total duration of 19.8 ks. We performed a
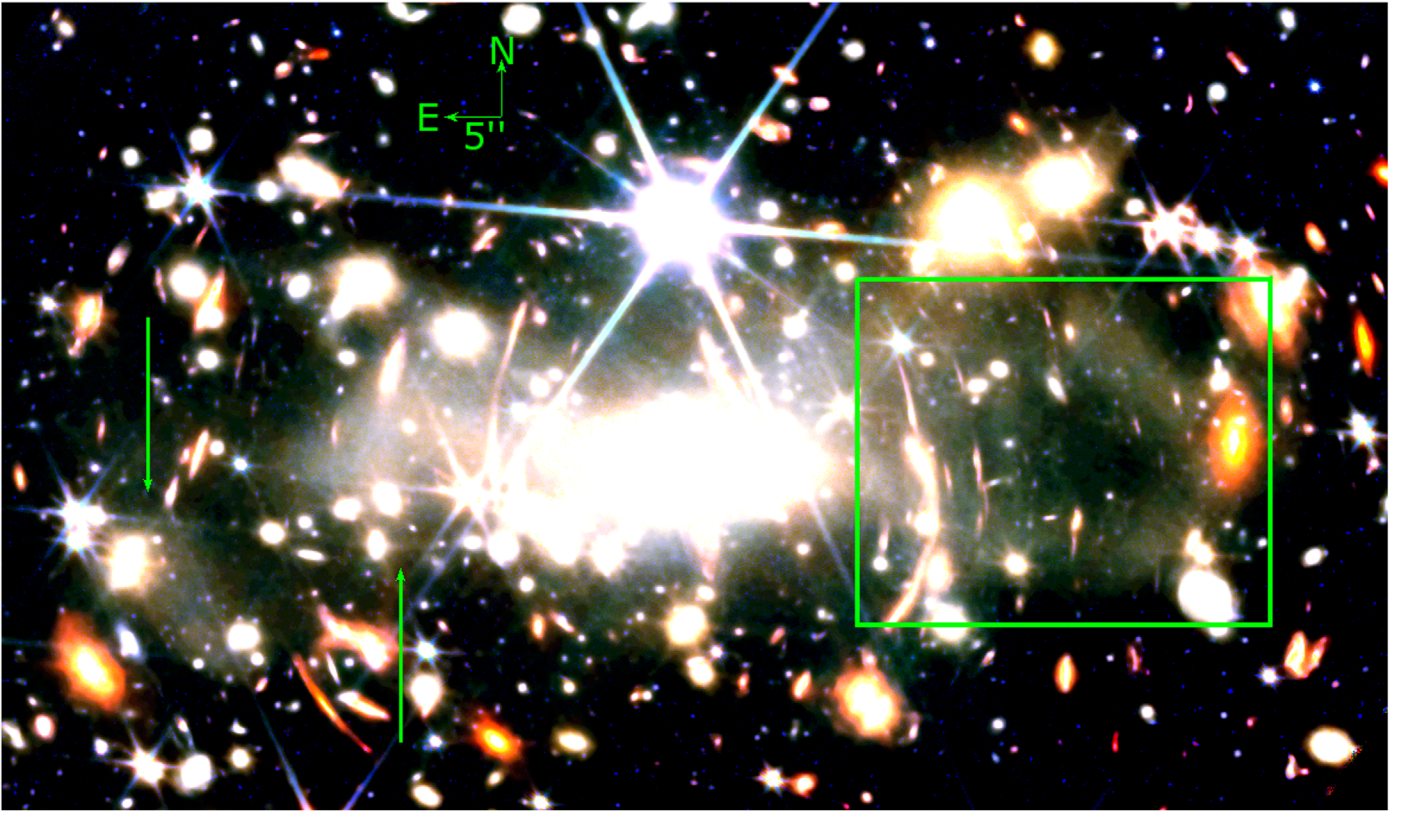
**Figure 2.** JWST/NIRCam image displayed at high contrast after median filtering with a sliding box spanning $21'' \times 21''$ to enhance low-surface-brightness features. Very faint, diffuse emission well beyond the BCG halo is highlighted in a rectangular area west of the cluster core. This image also shows smooth emissions marked by arrows.

standard reduction of the data using the CIAO[17] v4.13 (Fruscione et al. 2006) and CALDB v4.9.6 packages. We removed point sources detected either automatically by the WAVEDETECT routine or by visual inspection. Periods of background flares were removed by running the DEFLARE tool in the 9.5–12 keV band and for the whole energy range. We used the blank-sky background data associated with the observation as provided by the standard data-reduction pipeline.

## 4. Methods

### 4.1. Intracluster Light

The intracluster light (ICL) represents an important component of the cluster mass distribution. In addition, it is a unique tracer of a system's dynamical history and its underlying dark-matter distribution, as demonstrated in recent works (e.g., Montes & Trujillo 2014, 2022a, 2022b; Montes 2019; Deason et al. 2021; Gonzalez et al. 2021). While the ICL has so far proven extremely difficult to detect and study with ground- and space-based telescopes, the exceptional sensitivity of JWST's detectors holds great promise for the detection of these extended yet extremely low-surface-brightness features.

In order to enhance faint, diffuse emission, we apply a running-median filtering with a $21 \times 21$ pixel box size. The resulting image is shown in Figure 2.

---

### 4.2. Strong-lensing Mass Modeling

We derive a mass model for SMACS J0723 based on strong-lensing constraints identified in the cluster core, using the publicly available mass-modeling algorithm Lenstool (Jullo et al. 2007). We provide a short summary of our approach here and refer the reader to Kneib et al. (1996), Smith et al. (2005), Verdugo et al. (2011), and Richard et al. (2011) for more details. The cluster mass distribution is modeled as a series of parametric dual pseudo-isothermal ellipsoidal (dPIE; Elíasdóttir et al. 2007) dark matter halos with seven free parameters: the position $\Delta\alpha$, $\Delta\delta$ relative to a reference location; ellipticity $\epsilon$; position angle $\theta$; normalization $\sigma_{0,\mathrm{lt}}$; truncation radius $r_{\mathrm{cut}}$; and core radius $r_{\mathrm{core}}$. We use as input constraints the positions of prominent light peaks in each lensed image, as well as their spectroscopic redshifts where available (see Section 5.3) and large flat priors otherwise. The Lenstool algorithm uses a Monte Carlo Markov Chain (MCMC) formalism to explore the available parameter space and identifies the best fit as the set of parameter values that minimizes the scatter between the observed and predicted image-plane positions of the identified lensed features.

The lens plane is modeled as a combination of cluster-scale and galaxy-scale dPIE halos. For the cluster-scale dark matter halos, we fix the truncation radius ($r_{\mathrm{cut}}$) at 1500 kpc. This radius typically lies outside the strong-lensing region and therefore can not be well constrained using our model. We refer to Chang et al. (2018) and references therein for relevant insights on choosing this radius as the truncation radius. All other parameters are optimized unless indicated otherwise.
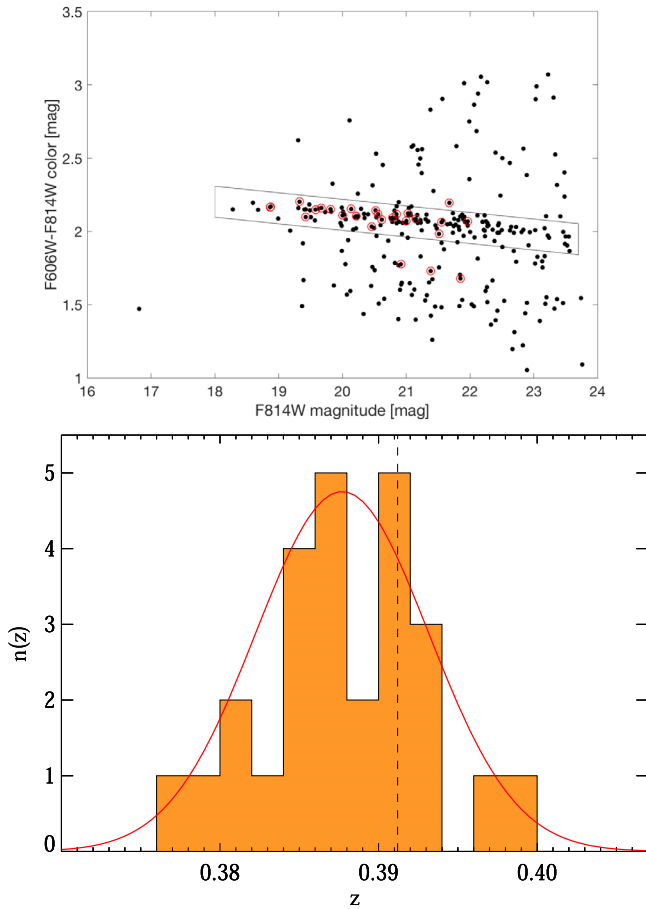
**Figure 3.** Top: color–magnitude diagram of galaxies in the field of view of SMACS J0723. The red sequence of cluster-member galaxies is clearly visible since the two filters used, F606W and F814W, straddle the Balmer break of massive elliptical galaxies at that redshift. The 26 spectroscopically confirmed cluster members from MUSE spectroscopy (open red circles) are overplotted. The rectangular shape shows the selection of the 144 cluster-member galaxies used in our lens model. Additionally, the four spectroscopically identified cluster members are included in our final cluster-member catalog. Bottom: histogram of the redshifts of the 26 cluster members identified spectroscopically within the MUSE data cube ranging from 0.3727 to 0.3981. Overlaid is the best Gaussian model which determines the cluster velocity dispersion. The vertical dashed line marks the location of the BCG in redshift space, $z_{\rm BCG} = 0.3912$, which is displaced from the systemic redshift of the cluster, $z = 0.3877$, corresponding to the mean redshift (see Section 5.1).

Galaxy-scale halos represent the contribution to the lensing potential from cluster-member galaxies (e.g., Natarajan & Kneib 1997; Jauzac et al. 2019; Sharon et al. 2020). Their positional parameters ($\Delta\alpha$, $\Delta\delta$; $\epsilon$; $\theta$) are fixed at their observed values as measured with Source Extractor (Bertin & Arnouts 1996; note that this subset includes ellipticity and position angle). The cluster-member catalog relies on HST photometry, as the two filters F606W and F814W (which straddle the Balmer break at the cluster redshift) provide a color gradient that allows us to isolate cluster-member galaxies that form the so-called red sequence (Gladders & Yee 2000), shown in Figure 3. We identify 144 galaxies. We also independently identify 26 cluster-member galaxies from MUSE spectroscopy ranging from $z = 0.3727$ to $z = 0.3981$ based on the clear overdensities in redshift, as shown in the histogram in Figure 3, and note that four of these fall outside the color range chosen for our red-sequence selection and where included in our cluster-member catalog.

To keep the number of optimized model parameters manageable in terms of computing time, we do not model the parameters of the galaxy-scale potentials individually but scale them to their observed $i$-band luminosity (using the Source Extractor output MAG_AUTO value) with respect to $L^*$ (mag$_{\rm F814W} = 19.12$), using a parameterized mass–luminosity scaling relation with a constant mass–luminosity ratio (see Natarajan & Kneib 1997 and Limousin et al. 2007, and discussions therein on the validity of this approach), leaving only the cut radius, $r_{\rm cut}$, and the fiducial central velocity dispersion, $\sigma_{0,\rm lt}$, free to vary. We note that $L^*$ is degenerate with the $\sigma_{0,\rm lt}$ normalization and offers flexibility. The BCG is modeled separately, since extremely luminous central cluster galaxies often do not follow the aforementioned general scaling relation (Newman et al. 2013a, 2013b). In addition, we separately model the cluster-member galaxy at (R.A. = 110.8402908 decl. = −73.4559518) which, being closest to the lensed image dubbed "The Sparkler" (image 2.2), has a disproportionate influence on the lens model (see Claeyssens et al. 2023 and Mowla et al. 2022, and references therein for a more detailed discussion of the Sparkler). Altogether, we thus jointly optimize 146 galaxies using our constant mass–luminosity relation.

The models we construct and present here are publicly available;[18] the linked-to website will be constantly updated.

### 4.3. X-Ray Analysis

To recover the properties of the gaseous intracluster medium (ICM) from the existing short Chandra X-ray observation of SMACS J0723, we model the spectrum of the emission with the Astrophysical Plasma Emission Code (APEC),[19] adopting abundance ratios as provided by Asplund et al. (2009). To account for foreground absorption, we complement this main spectral component with a photoelectric-absorption model.[20] The contribution from background emission is incorporated by creating an empirical model of the blank-sky background with B-spline functions whose coefficients were obtained through a fit of the blank-sky spectrum for the ACIS-I CCD on which the cluster is observed. We then keep the shape of the background spectrum constant in the fitting procedure and allow only its normalization to vary.

We perform all modeling within the SHERPA fitting environment (Freeman et al. 2001) combined with the Python wrapper of the MULTINEST nested-sampling package (Buchner et al. 2014; Feroz et al. 2019) to explore the parameter space of our model in the 0.5–8 keV energy band. As appropriate for the mostly low photon statistics per bin, we use a Poisson likelihood similar to CSTAT.[21] Depending on the fit, not all emission model parameters are left free to vary. We consider the background normalization a nuisance parameter and marginalize over it in our best-fit estimates for all physical model parameters.

### 5. Results

#### 5.1. Cluster Galaxies

In order to obtain an independent assessment of the dynamical state of SMACS J0723 as probed by the spatial and velocity distribution of the system's member galaxies, we

---

**Table 1**
R.A. and Decl. (J2000) as well as Redshifts of the 26 Cluster Members
Identified in the MUSE Observation of the Core of SMACS J0723

| R.A. (deg) | Decl. (deg) | z |
|---|---|---|
| 110.800 01 | −73.45269 | 0.3791 |
| 110.800 62 | −73.44852 | 0.3936 |
| 110.802 47 | −73.45867 | 0.3904 |
| 110.804 51 | −73.45615 | 0.3862 |
| 110.816 13 | −73.45119 | 0.3841 |
| 110.817 26 | −73.44940 | 0.3930 |
| 110.818 24 | −73.45462 | 0.3908 |
| 110.818 41 | −73.44827 | 0.3936 |
| 110.818 52 | −73.45524 | 0.3848 |
| 110.824 37 | −73.45991 | 0.3809 |
| 110.825 14 | −73.45454 | 0.3767 |
| 110.825 71 | −73.45869 | 0.3885 |
| 110.826 39 | −73.45499 | 0.3909 |
| 110.826 88 | −73.45463 | 0.3912 (BCG) |
| 110.832 69 | −73.45691 | 0.3867 |
| 110.836 83 | −73.45652 | 0.3981 |
| 110.837 63 | −73.45617 | 0.3895 |
| 110.837 80 | −73.45360 | 0.3864 |
| 110.840 09 | −73.45587 | 0.3908 |
| 110.845 64 | −73.45134 | 0.3845 |
| 110.848 75 | −73.46031 | 0.3970 |
| 110.853 10 | −73.45666 | 0.3838 |
| 110.853 78 | −73.45006 | 0.3844 |
| 110.855 06 | −73.45020 | 0.3864 |
| 110.855 74 | −73.45574 | 0.3815 |
| 110.856 26 | −73.45070 | 0.3872 |

examine the MUSE data cube and extract a catalog of 26 spectroscopically confirmed cluster members (Table 1).

Using the ROSTAT package of Beers et al. (1990) we derive an improved cluster redshift of $z = 0.3877$ for SMACS J0723 and determine the cluster velocity dispersion as $\sigma = 1180^{+160}_{-180}$ km s$^{-1}$. We show the corresponding redshift histogram in Figure 3. Within the statistical uncertainties set by the small sample size, the radial-velocity distribution exhibits no significant substructure indicative of an active merger along an axis that lies close to our line of sight. We note, however, that the radial velocity of the BCG is clearly offset from the centroid of the distribution; the implied peculiar velocity might reflect incomplete relaxation after a potentially recent line-of-sight merger.

### 5.2. Intracluster Light

We examine the filtered NIRCam image of SMACS J0723 shown in Figure 2 in search of unusual low-surface-brightness features, and note diffuse excess emission west of the cluster core but also past the far eastern extension of the ICL halo of the BCG. Although the physical nature and origin of such excess ICL are not immediately clear, we mark these areas as locations of potential minor mass concentrations within the cluster lens that are not associated with either overdensities of cluster members or excess X-ray emission and are thus not readily identifiable by other means.

### 5.3. Strong-lensing Constraints

The strong-lensing constraints for our lens models are given by the image-plane locations of multiple images of lensed sources, identified either in previous HST images or in the new JWST observations.
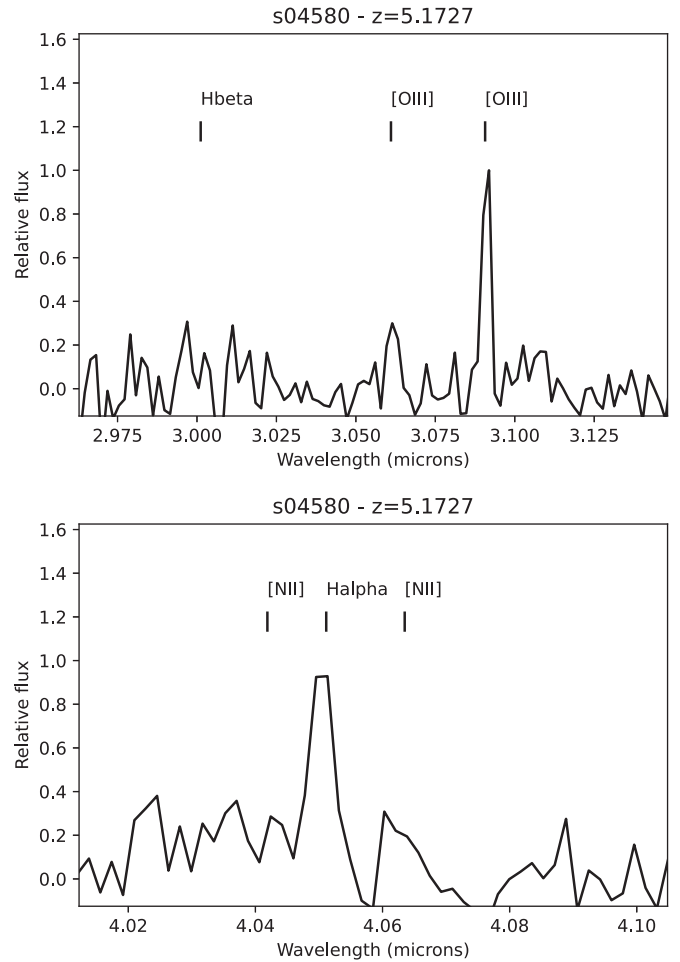


**Figure 4.** Identified emission lines in the NIRSpec/G395m spectrum of image 7.1. The detection of strong [O III]5007 Å and Hα lines, accompanied by weaker [O III]4959 Å and [N II] emission, makes this redshift determination robust.

Golubchik et al. (2022) identify five arc candidates in the field of SMACS J0723 and report three multiple-image systems that have spectroscopic redshifts. We confirm all of these in our examination of all available data and identify 16 additional multiple-image systems. Through careful inspection of the MUSE data cube (Section 3.2), we also secure an additional spectroscopic redshift for one of the systems photometrically identified by Golubchik et al. (2022): System 3 (at $z = 1.9914$).

Initial inspection of the NIRSpec MSA spectroscopic data yields an additional spectroscopic constraint by confirming a star-forming region in image 7.1 to be at $z = 5.1727$, the highest redshift of any spectroscopically confirmed multiple image in this cluster (Figure 4). We also confirm the redshift for the "Beret" galaxy (Figure 5), a highly stretched spiral galaxy that is only partially multiply imaged, as $z = 1.16$; however, we do not include this image as a modeling constraint.

All individual images are marked in Figure 5, and Table 2 summarizes the positions and spectroscopic redshifts where available. Although the identification of systems without spectroscopic confirmation for all individual images should in principle be considered tentative, we propose to adopt Systems 1, 2, and 3 as secure identifications, in view of their unique morphology, which is identical for all of their multiple images.
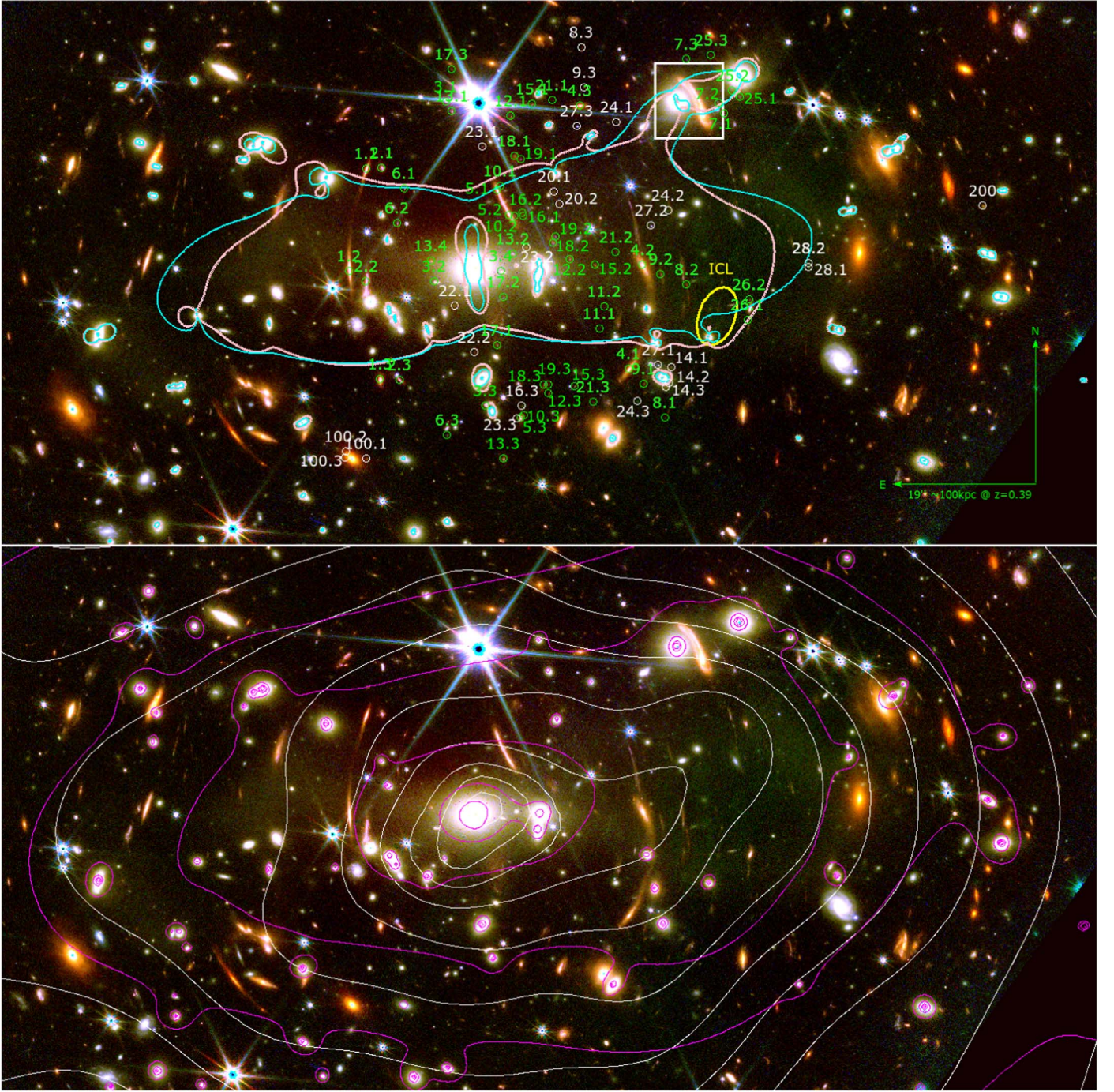
**Figure 5.** Top: color image of SMACS J0723 with multiple-image systems used in our models marked by green circles and all other candidates marked as white circles. Also shown are the critical curves for a source at redshift $z = 9$, in cyan for the single-component lens model and in pink for our final model that includes one additional mass clump marked by excess ICL at the location of the yellow ellipse. The white square highlights the "Beret" galaxy, a highly stretched spiral at $z = 1.16$ that is only partly multiply imaged (Section 5.3). Bottom: color image of SMACS J0723 with mass contours (in magenta) and X-ray surface-brightness contours (in white) overlaid. We note the visual similarity in ellipticity and asymmetrical distribution along the east–west axis.

## 5.4. Mass Distribution

### 5.4.1. Excess Mass

The presence of two bright galaxies northwest of the BCG motivates the inclusion of an additional large-scale halo in our model to better accommodate two nearby multiply imaged galaxies (Systems 7 and 25; see Section 5.3). Moreover, while we see no significant substructure in the distribution of cluster galaxies west and southwest of the BCG, we observe an extension of the ICL in these directions. The presence of this excess diffuse light (highlighted in Figure 2 and discussed in Sections 4.1 and 5.2) causes us to add a second large-scale mass component which proves crucial to reproducing the observed lensing geometry of Systems 8 and 26. Figure 5 shows the location of the additional component, referred to as the "ICL clump" in Table 3.

**Table 2**
Securely Identified Multiple-image Systems

| Sys. ID | R.A. (deg) J2000 | Decl. (deg) J2000 | $z$ | $\mu$ |
|---|---|---|---|---|
| 1.1 | 110.840 724 0 | −73.451 078 7 | 1.449 | $5.5^{+0.7}_{-0.6}$ |
| 1.2 | 110.842 948 9 | −73.454 839 9 | 1.449 | $11.4^{+2.1}_{-2.0}$ |
| 1.3 | 110.838 988 7 | −73.458 784 4 | 1.449 | $5.2^{+0.6}_{-0.5}$ |
| 2.1 | 110.838 728 8 | −73.451 050 8 | 1.3779 | $5.1^{+0.6}_{-0.5}$ |
| 2.2 | 110.840 777 1 | −73.455 212 2 | 1.3779 | $11.3^{+2.1}_{-1.9}$ |
| 2.3 | 110.836 498 3 | −73.458 813 6 | 1.3779 | $4.8^{+0.5}_{-0.5}$ |
| 3.1 | 110.830 503 6 | −73.448 631 2 | 1.9914 | $3.0^{+0.3}_{-0.2}$ |
| 3.2 | 110.831 998 8 | −73.455 202 2 | 1.9914 | $3.0^{+0.4}_{-0.3}$ |
| 3.3 | 110.825 439 3 | −73.459 776 7 | 1.9914 | $7.8^{+1.5}_{-0.8}$ |
| 3.4 | 110.823 389 3 | −73.454 835 0 | 1.9914 | $1.9^{+0.3}_{-0.3}$ |
| 4.1 | 110.806 998 2 | −73.458 430 8 | $2.31^{0.12}_{-0.10}$ | $6.9^{+0.6}_{-0.6}$ |
| 4.2 | 110.805 236 7 | −73.454 632 5 | ⋯ | $14.0^{+2.5}_{-1.9}$ |
| 4.3 | 110.813 288 1 | −73.448 786 9 | ⋯ | $4.4^{+0.4}_{-0.4}$ |
| 5.1 | 110.823 890 8 | −73.451 882 0 | 1.425 | $18.3^{+2.9}_{-2.4}$ |
| 5.2 | 110.822 352 9 | −73.452 783 1 | 1.425 | $20.0^{+3.0}_{-2.2}$ |
| 5.3 | 110.820 925 4 | −73.460 205 8 | 1.425 | $3.0^{+0.2}_{-0.2}$ |
| 6.1 | 110.835 854 0 | −73.451 819 9 | $1.70^{+0.04}_{-0.03}$ | $14.2^{+2.8}_{-2.1}$ |
| 6.2 | 110.836 761 1 | −73.453 086 8 | ⋯ | $12.7^{+1.5}_{-1.0}$ |
| 6.3 | 110.830 393 3 | −73.460 843 6 | ⋯ | $3.0^{+0.2}_{-0.2}$ |
| 7.1 | 110.794 760 4 | −73.449 097 5 | 5.17 | $20.3^{+9.9}_{-4.1}$ |
| 7.2 | 110.795 444 2 | −73.448 721 1 | 5.17 | $23.3^{+21.8}_{-6.7}$ |
| 7.3 | 110.799 603 9 | −73.447 086 6 | 5.17 | $5.4^{+1.0}_{-0.5}$ |
| 8.1 | 110.802 378 4 | −73.460 205 5 | $14.39^{+1.17}_{-2.11}$ | $4.7^{+0.9}_{-0.5}$ |
| 8.2 | 110.799 559 8 | −73.455 350 1 | ⋯ | $9.6^{+1.3}_{-1.8}$ |
| †8.3 | 110.813 056 4 | −73.446 665 1 | ⋯ | ⋯ |
| 9.1 | 110.805 063 7 | −73.458 965 6 | $3.01^{+0.25}_{-0.21}$ | $7.2^{+0.8}_{-0.8}$ |
| 9.2 | 110.802 889 6 | −73.454 956 4 | ⋯ | $16.0^{+4.5}_{-2.3}$ |
| †9.3 | 110.812 700 4 | −73.448 125 | ⋯ | ⋯ |
| 10.1 | 110.823 528 9 | −73.451 739 2 | $1.43^{+0.02}_{-0.02}$ | $15.2^{+2.5}_{-1.9}$ |
| 10.2 | 110.821 619 2 | −73.452 824 3 | ⋯ | $16.6^{+2.3}_{-1.9}$ |
| 10.3 | 110.820 511 9 | −73.460 115 2 | ⋯ | $3.0^{+0.2}_{-0.2}$ |
| 11.1 | 110.810 730 6 | −73.456 957 4 | $1.73^{+0.11}_{-0.09}$ | $23.5^{+7.3}_{-3.1}$ |
| 11.2 | 110.810 146 4 | −73.456 159 9 | ⋯ | $22.9^{+7.3}_{-3.8}$ |
| 12.1 | 110.822 136 4 | −73.449 150 4 | $1.81^{+0.07}_{-0.06}$ | $3.8^{+0.4}_{-0.3}$ |
| 12.2 | 110.814 617 9 | −73.454 411 9 | ⋯ | $3.6^{+0.5}_{-0.5}$ |
| 12.3 | 110.817 309 3 | −73.459 317 | ⋯ | $4.0^{+0.4}_{-0.3}$ |
| 13.1 | 110.829 722 4 | −73.448 990 7 | $3.34^{+0.49}_{-0.3}$ | $3.9^{+0.4}_{-0.3}$ |
| 13.2 | 110.821 915 | −73.454 206 7 | ⋯ | $3.3^{+0.5}_{-0.4}$ |
| 13.3 | 110.823 115 | −73.46170.5 | ⋯ | $3.0^{+0.2}_{-0.2}$ |
| 13.4 | 110.832 428 6 | −73.454 464 2 | ⋯ | $3.0^{+0.5}_{-0.4}$ |
| †14.1 | 110.801 556 8 | −73.458 354 6 | ⋯ | ⋯ |
| †14.2 | 110.801 814 8 | −73.458 948 | ⋯ | ⋯ |
| †14.3 | 110.802 227 | −73.459 084 3 | ⋯ | ⋯ |
| 15.1 | 110.819 389 5 | −73.448 743 6 | $2.04^{+0.09}_{-0.08}$ | $4.3^{+0.4}_{-0.4}$ |
| 15.2 | 110.811 381 3 | −73.454 623 5 | ⋯ | $5.1^{+0.6}_{-0.6}$ |
| 15.3 | 110.813 970 5 | −73.459 052 2 | ⋯ | $4.6^{+0.4}_{-0.4}$ |
| 16.1 | 110.820 62 | −73.452 718 1 | $1.09^{+0.03}_{-0.03}$ | $214.3^{+262.7}_{-23.5}$ |
| 16.2 | 110.820 525 | −73.452 815 6 | ⋯ | $205.1^{+235.3}_{-20.2}$ |
| †16.3 | 110.820 762 6 | −73.459 774 6 | ⋯ | ⋯ |

**Table 2**
(Continued)

| Sys. ID | R.A. (deg) J2000 | Decl. (deg) J2000 | $z$ | $\mu$ |
|---|---|---|---|---|
| 17.1 | 110.823 947 9 | −73.457 552 8 | $2.12^{+0.11}_{-0.09}$ | $15.3^{+2.7}_{-2.3}$ |
| 17.2 | 110.823 135 4 | −73.455 808 3 | ⋯ | $7.9^{+0.8}_{-0.8}$ |
| 17.3 | 110.829 776 9 | −73.447 461 9 | ⋯ | $2.5^{+0.2}_{-0.2}$ |
| 18.1 | 110.821 671 1 | −73.450 636 2 | $1.37^{+0.03}_{-0.03}$ | $5.7^{+0.7}_{-0.5}$ |
| 18.2 | 110.816 745 | −73.453 796 8 | ⋯ | $6.8^{+0.9}_{-0.7}$ |
| 18.3 | 110.817 934 | −73.459 010 1 | ⋯ | $3.7^{+0.3}_{-0.3}$ |
| 19.1 | 110.820 880 4 | −73.450 746 1 | $1.37^{+0.03}_{-0.03}$ | $6.3^{+0.3}_{-0.3}$ |
| 19.2 | 110.816 405 8 | −73.453 573 3 | ⋯ | $7.7^{+1.1}_{-0.8}$ |
| 19.3 | 110.817 304 6 | −73.458 994 2 | ⋯ | $3.7^{+0.3}_{-0.3}$ |
| †20.1 | 110.816 581 4 | −73.451 944 5 | ⋯ | ⋯ |
| †20.2 | 110.815 939 2 | −73.452 393 2 | ⋯ | ⋯ |
| 21.1 | 110.816 835 4 | −73.448 577 | $2.60^{+0.17}_{-0.14}$ | $4.1^{+0.4}_{-0.4}$ |
| 21.2 | 110.808 665 4 | −73.454 144 2 | ⋯ | $6.1^{+0.7}_{-0.7}$ |
| 21.3 | 110.811 582 7 | −73.459 644 6 | ⋯ | $4.2^{+0.3}_{-0.3}$ |
| †22.1 | 110.829 34 | −73.456 120 4 | ⋯ | ⋯ |
| †22.2 | 110.826863 | −73.457 816 1 | ⋯ | ⋯ |
| †23.1 | 110.825 836 3 | −73.450 283 9 | ⋯ | ⋯ |
| †23.2 | 110.820 161 2 | −73.453 978 9 | ⋯ | ⋯ |
| †23.3 | 110.821 397 5 | −73.460 231 4 | ⋯ | ⋯ |
| †24.1 | 110.808 570 8 | −73.449 408 3 | ⋯ | ⋯ |
| †24.2 | 110.801 957 9 | −73.452 632 2 | ⋯ | ⋯ |
| †24.3 | 110.805 892 1 | −73.459 599 7 | ⋯ | ⋯ |
| 25.1 | 110.792 703 8 | −73.448 481 4 | $3.93^{+1.65}_{-1.01}$ | $13.7^{+4.7}_{-2.5}$ |
| 25.2 | 110.793 684 2 | −73.448 243 9 | ⋯ | $10.6^{+4.0}_{-2.1}$ |
| 25.3 | 110.796 412 9 | −73.446 940 6 | ⋯ | $5.1^{+0.8}_{-0.6}$ |
| 26.1 | 110.791 708 9 | −73.456 633 2 | $2.88^{+1.35}_{-1.15}$ | $60.6^{+49.9}_{-31.7}$ |
| 26.2 | 110.791 491 3 | −73.455 897 3 | ⋯ | $64.8^{+77.8}_{-5.5}$ |
| †27.1 | 110.803 224 6 | −73.458 288 6 | ⋯ | ⋯ |
| †27.2 | 110.804 129 2 | −73.453 188 3 | ⋯ | ⋯ |
| †27.3 | 110.813 669 2 | −73.449 537 8 | ⋯ | ⋯ |
| †28.1 | 110.783 907 1 | −73.454 721 9 | ⋯ | ⋯ |
| †28.2 | 110.783 867 1 | −73.454 553 1 | ⋯ | ⋯ |
| †100.1 | 110.840 764 | −73.461 69 | ⋯ | ⋯ |
| †100.2 | 110.843 379 4 | −73.461 453 9 | ⋯ | ⋯ |
| †100.3 | 110.843 516 | −73.461 665 8 | ⋯ | ⋯ |
| †200 | 110.761 503 3 | −73.452 474 7 | ⋯ | ⋯ |

**Note.** "System" specifies the group of images originating from the same source galaxy, whereas "ID" refers to the name of the individual image. "R.A." and "Decl." are the R.A. and decl. (J2000) of the image. $z$ is the measured spectroscopic redshift. Redshifts with error bars denote the median model-optimized redshift and the 68% confidence interval. Systems with † symbols are not used as constraints in this model. $\mu$ is the magnification at the location of the observed constraints. Where errors are listed for $\mu$, the cited values are the median magnification and the 68% confidence interval from the lens-model optimization.

To assess the importance of this additional component to our mass model, we run two models with parameters as listed in Table 3: one with only a cluster-scale halo around the BCG (comparison model in Table 3), and another one including the additional large-scale halos described above (fiducial model in

**Table 3**
Candidate Lens Models and Output Parameters

| Model Name (Fit Statistics) | Component | $\Delta\alpha$[a] (″) | $\Delta\delta$[a] (″) | $\varepsilon$[b] | $\theta$ (deg) | $\sigma_{0,\mathrm{lt}}$[c] (km s$^{-1}$) | $r_{\mathrm{cut}}$ (kpc) | $r_{\mathrm{core}}$ (kpc) |
|---|---|---|---|---|---|---|---|---|
| Fiducial model | Cluster halo | $2.82^{+0.92}_{-0.9}$ | $1.31^{+0.25}_{-0.22}$ | $0.67^{+0.05}_{-0.05}$ | $8.1^{+0.77}_{-0.71}$ | $983.32^{+31.85}_{-35.39}$ | [1500.0] | $17.96^{+1.45}_{-1.44}$ |
| rms = 0″32 $k = 46$ | BCG | [0.0] | [0.0] | ⋯ | [29.2] | $292.09^{+23.36}_{-19.75}$ | $56.39^{+25.86}_{-32.54}$ | $0.44^{+0.42}_{-0.28}$ |
| $\chi^2/\nu = 1.0$, dof $= 32$ | NW clump[d] | $-30.8^{+1.63}_{-1.8}$ | $22.28^{+1.48}_{-0.79}$ | $0.35^{+0.29}_{-0.24}$ | $6.53^{+58.6}_{-70.74}$ | $154.59^{+24.27}_{-29.65}$ | $34.77^{+13.53}_{-17.14}$ | $0.92^{+0.56}_{-0.5}$ |
| $\log(\mathcal{L}) = -28$ | ICL clump | $-34.51^{+2.29}_{-5.52}$ | $-5.4^{+1.97}_{-1.12}$ | $0.5^{+0.23}_{-0.21}$ | $40.9^{+20.81}_{-16.81}$ | $375.86^{+51.21}_{-55.89}$ | $158.97^{+22.02}_{-45.46}$ | $7.07^{+1.83}_{-3.71}$ |
| $\log(\mathcal{E}) = -133$ | CM gal.[e] | [13.64] | [−4.42] | $0.31^{+0.2}_{-0.21}$ | $-0.42^{+62.04}_{-62.99}$ | $26.91^{+32.69}_{-18.62}$ | $19.77^{+12.51}_{-12.53}$ | $1.02^{+0.59}_{-0.66}$ |
| BIC $= 256$ AICc $= 287$ | $L^*$ galaxy | ⋯ | ⋯ | ⋯ | ⋯ | $144.8^{+13.1}_{-11.9}$ | $67.5^{+20.6}_{-18.5}$ | [0.15] |
| Comparison model | Cluster halo | $-4.44^{+2.12}_{-2.05}$ | $1.04^{+0.4}_{-0.41}$ | $0.86^{+0.03}_{-0.04}$ | $183.86^{+0.68}_{-0.71}$ | $1079.89^{+44.21}_{-37.73}$ | [1500.0] | $21.69^{+3.34}_{-2.91}$ |
| rms = 0″85 $k = 39$ | BCG | [0.0] | [0.0] | ⋯ | [29.2] | $362.25^{+27.57}_{-25.55}$ | $12.54^{+3.1}_{-3.39}$ | $0.28^{+0.2}_{-0.2}$ |
| $\chi^2/\nu = 1.0$, dof $= 39$ | NW clump[d] | $-28.35^{+1.81}_{-2.26}$ | $22.38^{+2.14}_{-1.4}$ | $0.28^{+0.23}_{-0.15}$ | $-5.79^{+61.23}_{-56.0}$ | $268.71^{+20.96}_{-29.54}$ | $57.71^{+22.77}_{-19.9}$ | $4.06^{+5.56}_{-2.77}$ |
| $\log(\mathcal{L}) = -142$ | CM gal.[e] | [13.64] | [−4.42] | $0.54^{+0.31}_{-0.36}$ | $4.21^{+59.91}_{-66.9}$ | $91.83^{+40.79}_{-51.69}$ | $19.68^{+12.22}_{-13.28}$ | $0.58^{+0.25}_{-0.26}$ |
| $\log(\mathcal{E}) = -202$ | $L^*$ galaxy | ⋯ | ⋯ | ⋯ | ⋯ | $169.6^{+38.1}_{-36.3}$ | $48.7^{+17.9}_{-23.3}$ | [0.15] |
| BIC $= 454$ AICc $= 444$ | ⋯ | ⋯ | ⋯ | ⋯ | ⋯ | ⋯ | ⋯ | ⋯ |

**Notes.** Quantities in brackets are fixed parameters. Other output quantities are the median value and the 68% confidence interval from the model optimization.
[a] $\Delta\alpha$ and $\Delta\delta$ are the relative position to the reference coordinate point: ($\alpha = 110.82675$, $\delta = -73.454628$).
[b] Ellipticity ($\varepsilon$) is defined to be $(a^2 - b^2)/(a^2 + b^2)$, where $a$ and $b$ are the semimajor and semiminor axes of the ellipse.
[c] $\sigma_{0,\mathrm{lt}}$ is the normalization parameter and represents a fiducial central velocity dispersion as defined in the dPIE parameterization within Lenstool.
[d] "NW clump" refers to the additional northwestern clump near systems 7 and 25 and the galaxy nicknamed "the Beret."
[e] "CM gal." refers to the galaxy near System 2.2 ("the Sparkler").
[f] $k$ is the number of free parameters in the model.

Table 3). Proceeding in our analysis, as described below, we only use the most complex model since it provides a better overall rms and Bayesian information criterion (BIC; Schwarz 1978), both criteria used in previous works (e.g., Acebron et al. 2017; Collett et al. 2017; Lam et al. 2018).

### 5.4.2. Comparison with Other Mass Models

We compare the results of our improved strong-lensing analysis with models from previous works on SMACS J0723. Two of these are from the public release of RELICS cluster models (Coe et al. 2019), derived using the GLAFIC lens-mapping package and a Lenstool model detailed in Sharon et al. (2023), respectively. In addition, we compare our results with those from the recent analysis by Golubchik et al. (2022), performed using the Light Traces Mass (LTM) software.

Table 4 lists and compares the masses from all existing lens models for SMACS J0723 at three different radii: 128, 200, and 400 kpc. Here, 128 kpc corresponds to the largest cluster-centric distance of the strong-lensing constraints commonly used by all models (this multiple-image system is labeled System 4 in our analysis). The masses within 200 kpc can be compared to those from the larger study by Fox et al. (2022) on 74 different clusters, whereas the radius of 400 kpc is the largest radius shared by all mass maps. Golubchik et al. (2022) also cite masses at two additional radii, corresponding to the Einstein radii derived with their model for source redshifts of $z = 1.45$ and $z = 2$: $M_{\mathrm{Golubchik+22,78\,kpc}} = (3.42 \pm 0.47) \times 10^{13}\,M_\odot$ and $M_{\mathrm{Golubchik+22,90\,kpc}} = (4.15 \pm 0.58) \times 10^{13}\,M_\odot$, respectively. Our model yields higher masses of $M_{78\,\mathrm{kpc}} = (3.81 \pm 0.02) \times 10^{13}\,M_\odot$, and $M_{90\,\mathrm{kpc}} = (4.83 \pm 0.03) \times 10^{13}\,M_\odot$. Although these two masses are statistically consistent with each other, the discrepancies may also reflect differences in modeling assumptions and our addition of spectroscopic redshifts. The full profile shown in Figure 6 highlights the differences between the various mass profiles. At about 300 kpc, the mass density for the LTM lens model falls significantly below other measurements.

**Table 4**
Total Enclosed Cluster Mass at Different Radii

| Model | $M_{128\,\mathrm{kpc}}$ | $M_{200\,\mathrm{kpc}}$ | $M_{400\,\mathrm{kpc}}$ |
|---|---|---|---|
| This work | $81.27^{+0.76}_{-0.33}$ | $153.75^{+1.95}_{-0.78}$ | $348.14^{+6.59}_{-3.1}$ |
| RELICS-Lenstool | $80.8 \pm 0.7$ | $146.1 \pm 2.1$ | $323^{+8}_{-6}$ |
| RELICS-GLAFIC | $79.1^{+2.5}_{-1.6}$ | $144.1^{+6.5}_{-5.5}$ | $338^{+26}_{-25}$ |
| LTM | $68.6^{+0.5}_{-0.7}$ | $117.3^{+1.1}_{-1.9}$ | $276.9^{+5.8}_{-5.6}$ |

**Note.** In units of $10^{12}\,M_\odot$.

We note that Golubchik et al. (2022) report a high rms uncertainty of 2″3, whereas the rms of the RELICS model of 0″58 (Sharon et al. 2023) is typical for similar cluster-lens models based on a fairly limited number of multiple-image systems. By contrast, our new models (which employ many more strong-lensing constraints) yield an rms of 0″32. This trend is in line with an analysis of simulated clusters (Johnson & Sharon 2016), which shows that models with a large number of spectroscopic constraints yield more accurate strong-lensing magnifications and masses.

Following the release of the ERO data, two other teams (Caminha et al. 2022; Pascale et al. 2022) published lens models for SMACS J0723. We collaborated with both teams to work toward a set of mutually agreed-upon multiple-image constraints and labels. Here, we present a brief discussion and comparison of the remaining main differences between the three lens models.

We note that Caminha et al. (2022) present a spectroscopic redshift for System 19 of 1.3825. Due to the low signal-to-noise ratio of the detection and the presence of a skyline on top of the emission, we did not use this redshift as an input constraint in our modeling. We do, however, find a redshift of $1.42^{+0.02}_{-0.02}$ (consistent with theirs) from our fiducial model. As for the rms of each team's best lens model, Caminha et al. (2022)
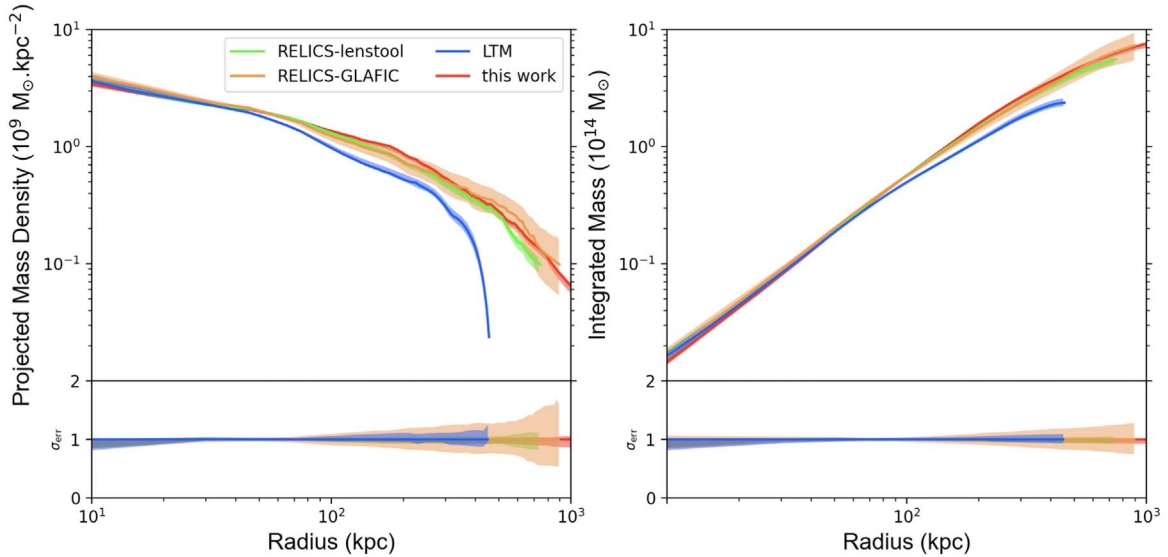
**Figure 6.** Left: mass–density profiles of SMACS J0723 obtained by our analysis (red) and in previous works: RELICS-LENSTOOL (green), RELICS-GLAFIC (orange), and LTM (blue) with their respective $1\sigma$ uncertainties (shaded areas). Right: integrated mass profiles obtained for SMACS J0723. The graph at the bottom of either panel shows the respective relative $1\sigma$ uncertainties of each model. As expected, these uncertainties are smallest within the radial range within which most strong-lensing constraints are observed.

report $0\rlap{.}''51$ and Pascale et al. (2022) quote $0\rlap{.}''93$, compared to our value of $0\rlap{.}''32$. Since this work and the analysis by Caminha et al. (2022) use the same modeling software (Lenstool), the difference between our models is due to our inclusion and reliance on a larger (also different) number of constraints and their additional use of an external shear component, while we instead include additional mass components, one of them motivated by the detection of excess ICL.

Caminha et al. (2022) report an ellipticity for the main cluster-scale halo of 0.51, whereas our comparison model (without ICL clump) has a median ellipticity of 0.86. Although the difference can partly be attributed to differences in the lensing constraints used, we stress that the ellipticity can also be reduced by the external shear component added in the model of Caminha et al. (2022). Our fiducial model (with the ICL clump) presents a lower median ellipticity of 0.67. A more detailed comparison, quantifying, for instance, the influence of each strong-lensing constraint on the model's ellipticity, is beyond the scope of this paper.

### 5.4.3. Dynamical State of SMACS J0723

The distribution of cluster members in SMACS J0723 reveals no significant substructure, neither in velocity space (see Section 5.1) nor in projection onto the plane of the sky, suggesting that the mass distribution is adequately described by a single cluster-scale component. However, in order to recover the geometry of multiple images newly discovered in the JWST observations (i.e., to minimize the rms of our model), we require a more sophisticated mass model that incorporates two additional diffuse mass concentrations, as discussed in Section 5.4.1. These could be interpreted as remnant/tracers of past dynamical activity in the cluster. We stress that our final mass model, which includes the aforementioned additional components, has an rms of $0\rlap{.}''32$, a substantial improvement over the value of $1\rlap{.}''26$ for a model which only includes a single cluster-scale halo centered on the BCG.

As discussed in Section 5.1, the distribution of the radial velocities of the cluster galaxies does not show compelling evidence of substructure along the line of sight. However, the offset between the radial velocity of the BCG and the centroid of the overall redshift distribution suggests that SMACS J0723 is not fully relaxed, an assessment that is supported by the complex mass distribution required and obtained from our strong-lensing analysis.

We report a large ellipticity of 0.86 for our comparison model (without ICL clump). By contrast, our fiducial model (with ICL clump) features an ellipticity of only 0.67. The fact that the addition of a mass component associated with the ICL reduces the overall ellipticity lends further support to the interpretation that the cluster is not relaxed. Some previous studies have also used external shear to motivate an additional mass component (Mahler et al. 2018) that also affects the ellipticity. Since the impact and interplay between components in the context of cluster-relaxation assessments remains an active area of exploration (Zitrin et al. 2015; Desprez et al. 2018; Lagattuta et al. 2019; Ghosh et al. 2021), we defer a more in-depth investigation of the cluster state to future work.

Additional evidence for dynamic activity and ongoing cluster evolution is provided by the presence of the excess ICL itself, shown in Figure 2. As discussed in Section 5.4.1, these ICL features play an important role for our lens-modeling efforts: without the presence of ICL revealed by the JWST ERO data, refinements to our mass model in the west and southwest regions would have been driven solely by statistics, i.e., the need to lower the rms, rather than being supported and motivated by physical evidence for the presence of mass in these regions of SMACS J0723.

### 5.5. Magnification Measurements

Thanks to the dramatically increased number of multiple-image systems uncovered with JWST, as well as the availability of partial spectroscopic coverage to anchor the mass and shape of the cluster lens, we are able to derive magnification maps for SMACS J0723 across the footprints of
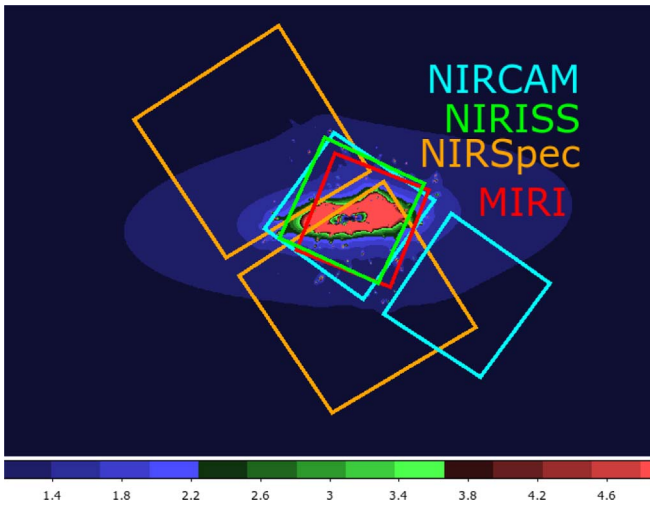
**Figure 7.** Magnification map obtained from our mass model for a source at redshift $z = 9$. Overlaid are the footprints of JWST's instruments.



**Figure 8.** Surface area in the source plane within a $300''$ box centered on the cluster at a magnification above a given threshold $\mu$ for a source at $z = 9$. We here compare the values obtained with our updated mass model with those from the RELICS-LENSTOOL model.

all JWST instruments. Figure 7 shows the magnification map obtained for sources at redshift $z = 9$.

Following the method presented by Wong et al. (2012) and subsequently applied to HFF analyses (e.g., Jauzac et al. 2014, 2015; Lam et al. 2014; Wang et al. 2015; Hoag et al. 2016), we use the surface area in the source plane, $\sigma_\mu$, above a given magnification factor, $\mu$, as a metric to quantify the efficiency of the lens to magnify high-redshift background galaxies, noting that $\sigma_\mu$ is directly proportional to the unlensed comoving volume covered at high redshift at a given magnification $\mu$.

Figure 8 shows the evolution of $\sigma_\mu(>\mu)$ as a function of the magnification obtained from our final mass model of SMACS J0723 for a source at a redshift $z = 9$. Our model yields $\sigma_\mu(\mu > 3) = 1.52$ arcmin$^2$, $\sigma_\mu(\mu > 5) = 1.0$ arcmin$^2$, and $\sigma_\mu(\mu > 10) = 0.7$ arcmin$^2$. Table 5 compares these values with measurements obtained by RELICS-Lenstool, i.e., with the same mass-modeling algorithm. The pre-JWST RELICS-Lenstool model used seven unique systems as constraints, with no spectroscopic redshifts, and yielded smaller areas than found from the model presented in this paper, especially at very high magnifications, suggesting that SMACS J0723 is a more powerful cluster lens than initially believed.

As a general caveat regarding magnification maps, we acknowledge limitations caused by a lack of constraints at large cluster-centric distances. We note, however, that the wide-angle X-ray observation performed with Chandra's ACIS-I detector (discussed in Sections 4.3 and 5.6) does not reveal any further sources indicative of gravitationally collapsed mass concentrations in the vicinity of SMACS J0723. We therefore consider our magnification maps (and the associated error maps) to be robust and make them available to the community as part of this publication. We acknowledge that magnification values beyond the region where multiple images reside result from a model extrapolation and could be affected by systematic uncertainties.

### 5.6. Intracluster Medium

#### 5.6.1. X-Ray Morphology

Figure 1 shows isointensity contours of the adaptively smoothed X-ray surface brightness from SMACS J0723 overlaid on the JWST color image of the cluster core. We find the X-ray emission to feature a well defined single peak at a
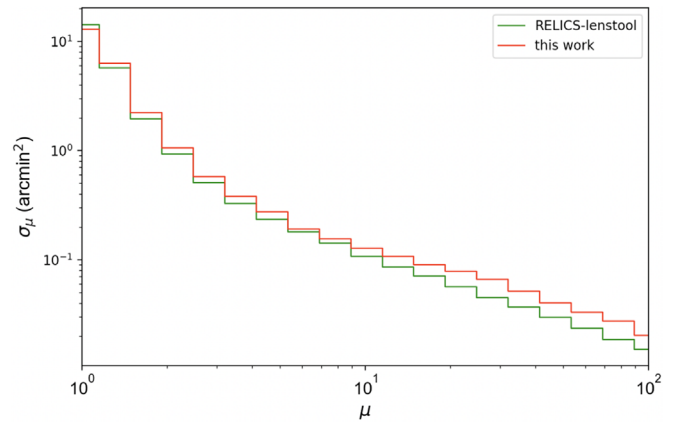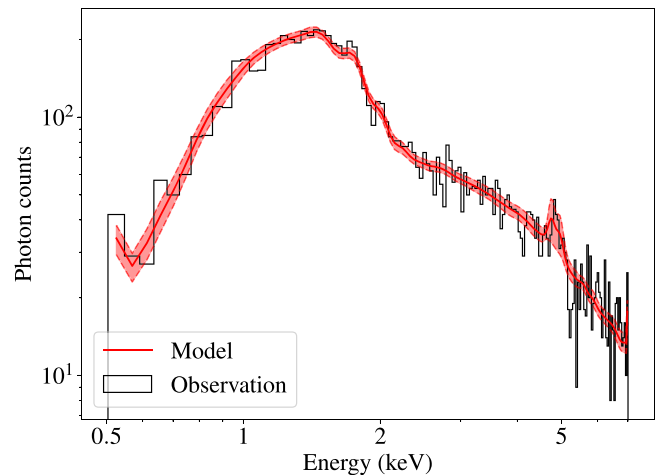


**Figure 9.** Global spectrum of the observed ICM emission within 1 Mpc of the X-ray peak, corresponding to approximately $r_{1000}$ (the radius enclosing a thousand times the mean density of the universe at that redshift). Overlaid in red is the best-fit APEC model with its associated 68% confidence range.

**Table 5**
Surface Area $\sigma_\mu$ in the Source Plane with Magnifications in Excess of a Given Magnification $\mu$ for this Work and the RELICS-Lenstool

| Model | $\sigma_\mu(3)$ | $\sigma_\mu(5)$ | $\sigma_\mu(10)$ |
|---|---|---|---|
| This work | 1.52 | 1.0 | 0.7 |
| RELICS-Lenstool | 1.5 | 0.95 | 0.5 |

**Note.** We quote $\sigma_\mu(>\mu)$ for $\mu = 3$, 5, and 10 for a source at redshift $z = 9$. The RELICS-Lenstool is published in Sharon et al. (2023).

location that coincides perfectly with that of the BCG.[22] While such alignment can be viewed as a sign of a system in dynamic equilibrium, the clearly disturbed X-ray morphology outside the very core region represents unambiguous evidence of recent merger activity.

---

[22] Although a direct astrometric alignment of the JWST and Chandra images is precluded by the fact that all X-ray point sources detected in the Chandra observations fall outside the JWST field of view, a comparison with wide-field *J*-band imaging obtained by the VISTA Hemisphere Survey (ESO Progamme 179.A-2010; PI: McMahon) limits the relative astrometric misalignment to about $1''$.
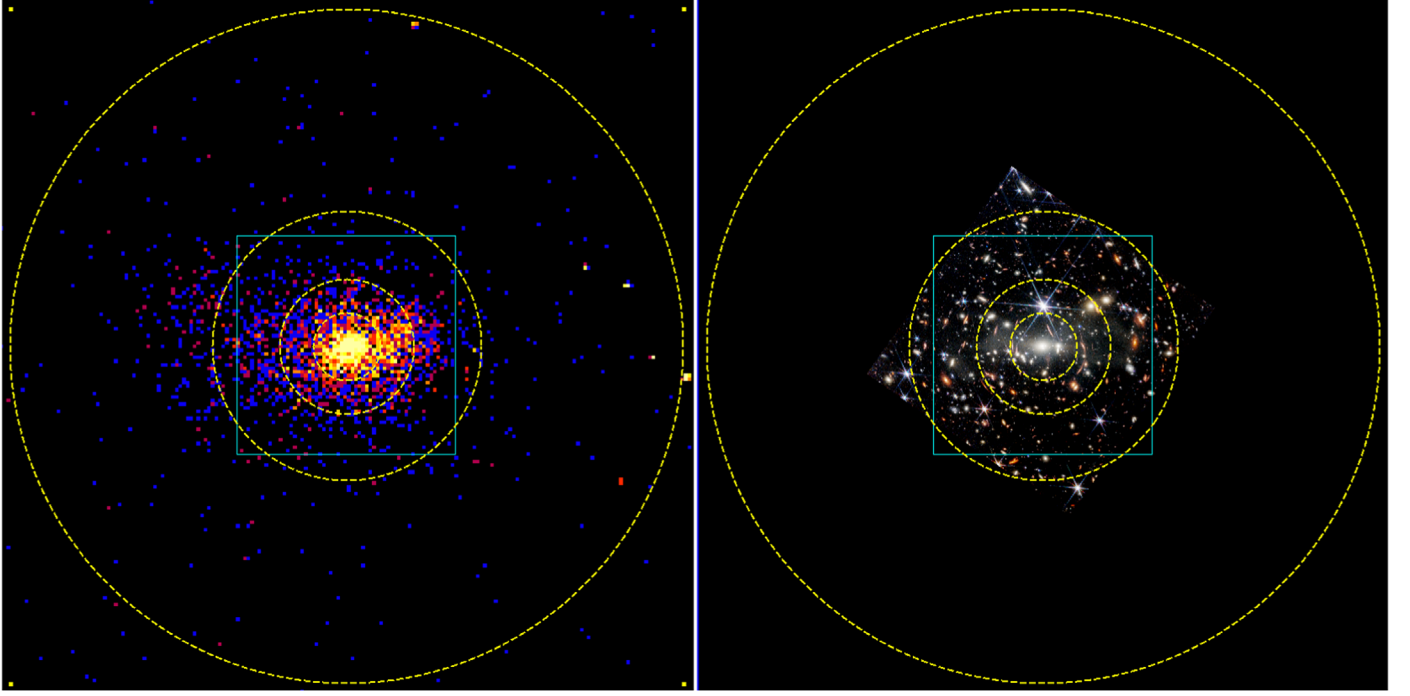
**Figure 10.** Regions of interest for our measurements of the ICM temperature overlaid on the Chandra ACSI-I image of SMACS J0723 (left; 2″ pixels, 0.5–7 keV, logarithmic intensity scaling) and on the JWST image of the system (right). The dashed circles have radii of 100, 200, 400, and 1000 kpc, respectively, at the cluster redshift. The cyan square marks the region shown in Figure 1.
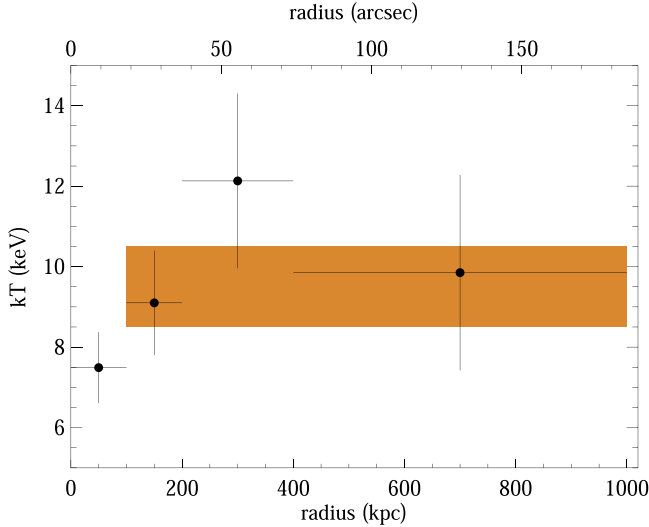


**Figure 11.** ICM temperature measurements within the regions shown in Figure 10; vertical bars represent $1\sigma$ uncertainties, horizontal bars represent the width of the respective annulus. The ambient ICM temperature in the combined regions beyond $r = 100$ kpc (i.e., within the annulus from 200 to 1000 kpc) with its $1\sigma$ error is shown as an orange rectangle.

### 5.6.2. Intracluster Medium Temperature

The spectral analysis summarized in Section 4.3 yields a global ICM temperature (within 1 Mpc of the X-ray peak) $kT = 9.80^{+1.54}_{-1.37}$ keV, a metallicity $Z = 0.38^{+0.12}_{-0.11}\,Z_\odot$, and an equivalent hydrogen column density $n_H = 1.94^{+0.03}_{-0.03} \times 10^{21}$ cm$^{-2}$. Figure 9 shows the global spectrum as well as the best-fit spectral model with 68% uncertainties (as represented by the associated subset of the sampled parameter distributions). Our best-fit value for $n_H$ agrees to better than $1\sigma$ with the total

**Table 6**
Global X-Ray Properties of SMACS J0723 Computed within $r = r_{1000}$

| | R.A., decl. (J2000) | $kT$ (keV) |
|---|---|---|
| | 07:23:18.0 −73:27:19 | $9.8^{+1.5}_{-1.4}$ |
| Energy band | $f_X$ ($10^{-13}$ erg s$^{-1}$ cm$^{-2}$) | $L_X$ ($10^{44}$ erg s$^{-1}$) |
| 0.1–2.4 keV | $32.1^{+1.2}_{-1.1}$ | $18.6^{+0.7}_{-0.6}$ |
| 0.5–2 keV | $23.2^{+0.9}_{-0.8}$ | $13.4 \pm 0.5$ |
| 0.5–7 keV | $58.2 \pm 1.3$ | $33.6 \pm 0.8$ |
| 2–10 keV | $43.6^{+2.5}_{-2.6}$ | $25.2^{+1.4}_{-1.5}$ |
| Bolometric | $73.3 \pm 2.3$ | $42.4^{+1.4}_{-1.3}$ |

**Note.** Unabsorbed fluxes and total luminosities are both point-source corrected.

hydrogen (i.e., H I and H II) column density of $2.21 \times 10^{21}$ cm$^{-2}$ measured by Willingale et al. (2013).

We attempt to constrain spatial variations in the ICM temperature by fitting separate spectral models to the data in the regions marked in Figure 10. Acknowledging the reduced signal in these smaller regions, we adopt the Galactic total $n_H$ value; we also freeze the metallicity at $Z = 0.3$ for these fits, in agreement with typical metal-abundance values observed for nonrelaxed clusters at similar redshift (Ettori et al. 2015). The results, shown in Figure 11, are consistent with a constant ICM temperature but suggest (at less than $2\sigma$ significance) a slight drop in $kT$ in the very core of SMACS J0723.

### 5.6.3. Gas Mass

We perform a multiscale deprojection of the gas density and gas mass using the PYPROFFIT Python package, developed by Eckert et al. (2020). The analysis uses counts and background maps in the 0.5–2 keV energy band, an associated monochromatic
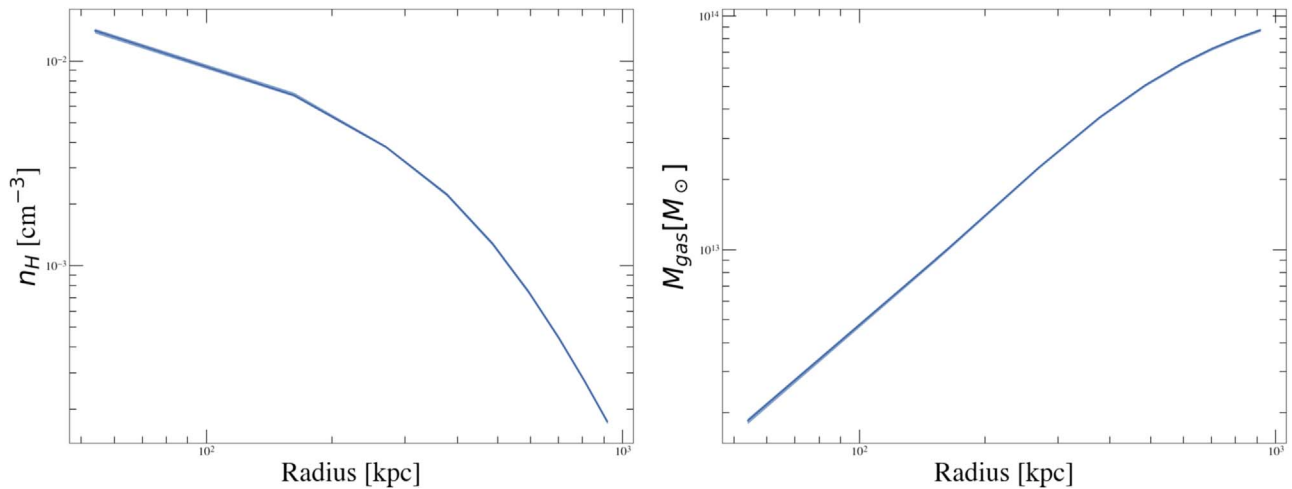
**Figure 12.** Profiles of the ICM density (left) and the cumulative gas mass (right) as determined from a spherical-deprojection analysis.

exposure map for an energy of 1.2 keV, as well as the values from our best-fit spectral model. The resulting profiles of the ICM density and the cumulative gas mass are shown in Figure 12 and place the total gas mass of SMACS J0723 at almost $10^{14} M_\odot$. A comparison with the total gravitational mass derived from our lens model (Figure 6 and Table 4) yields a gas-mass fraction of just under 10% for the cluster core, typical of massive clusters in general. A more detailed investigation of, for example, the baryon fraction across the system would require a significantly deeper X-ray observation and much more sophisticated spatial modeling of the ICM.

### 5.6.4. Global Properties

For reference, we summarize all global cluster properties derived for SMACS J0723 from the only existing, dedicated X-ray observation of the cluster in Table 6. All values are computed from the emission within $r = 1$ Mpc, which is very close to $r_{1000}$.

With a total X-ray luminosity well in excess of $10^{45}$ erg s$^{-1}$ in the ROSAT energy band (0.1–2.4 keV) in which the system was originally discovered (see Section 2), the properties of SMACS J0723 established here are a testament to the power of X-ray selection of clusters in general, and of the MACS project in particular, to uncover exceptionally massive clusters that stand to advance our understanding of a broad range of science topics, from cluster formation and evolution to lensing-assisted, ever-deeper views of the distant universe.

## 6. Discussion and Conclusion

We create and make available to the scientific community a robust strong-lensing mass model of the galaxy cluster SMACS J0723 at $z = 0.39$, the first strong-lensing cluster to be observed with JWST. Our model uses JWST ERO data, as well as archival, multiwavelength data of the cluster, from optical to X-ray wavelengths, and combines both imaging and spectroscopic observations. We identify 17 new multiple-image systems. We report a total number of 30 candidate multiple-image systems, two of which are isolated galaxy–galaxy lensed sources. Of the final 28 cluster-wide multiple-image systems, we use 21, namely 19 robust systems and two additional candidates located near the intracluster light concentrations identified by us. Our best-fit mass model contains only one

large cluster-scale halo and includes one diffuse large-scale halo that accounts for mass traced by the cluster ICL. Additional halos have masses closer to galaxy-scale halos. These halos bring flexibility to our model to adjust their nearby multiple-image systems. As a result, our model is able to reproduce overall the positions of the strong-lensing features to within 0″32 (rms).

The mentioned excess stellar cluster light (low-surface-brightness features that appear clearly on large scales and are enhanced in the JWST imaging by median filtering) may represent the signature of a recent merger event. Indeed, the combined evidence from our analysis of the overall mass distribution, radial velocities of cluster galaxies, and ICM properties also suggests that SMACS J0723 recently underwent a merger along an axis close to our line of sight but is well on its way to relaxation, as reflected in the nearly perfect alignment of the X-ray peak with the BCG and the overall mass distribution, as well as the increased ICM cooling in an emerging compact gaseous cluster core.

By combining greatly increased sensitivity with broad spectral coverage and spectacular spectroscopic capabilities, JWST's observation of SMACS J0723 reveals exquisite panchromatic details that not only dramatically facilitate the identification of multiple images of galaxies at redshift greater than 5 but also provide additional leverage to constrain the dynamical and merger history of clusters.

## Appendix
## Multiple Images

Images of the identified multiply-imaged systems are presented in Figure 13 and Figure 14.
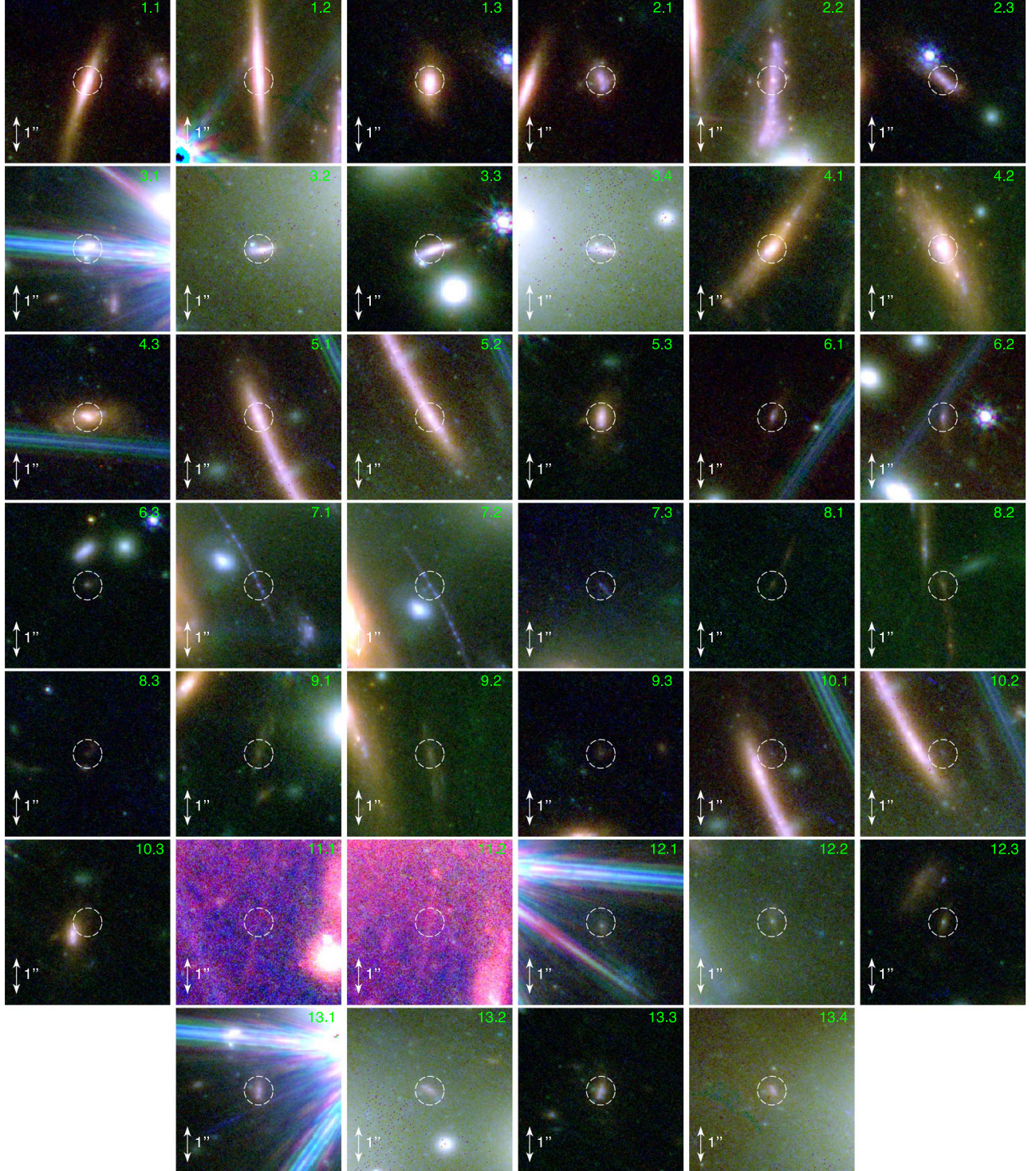


**Figure 13.** Thumbnails of multiply-imaged sources behind SMACS J0723.
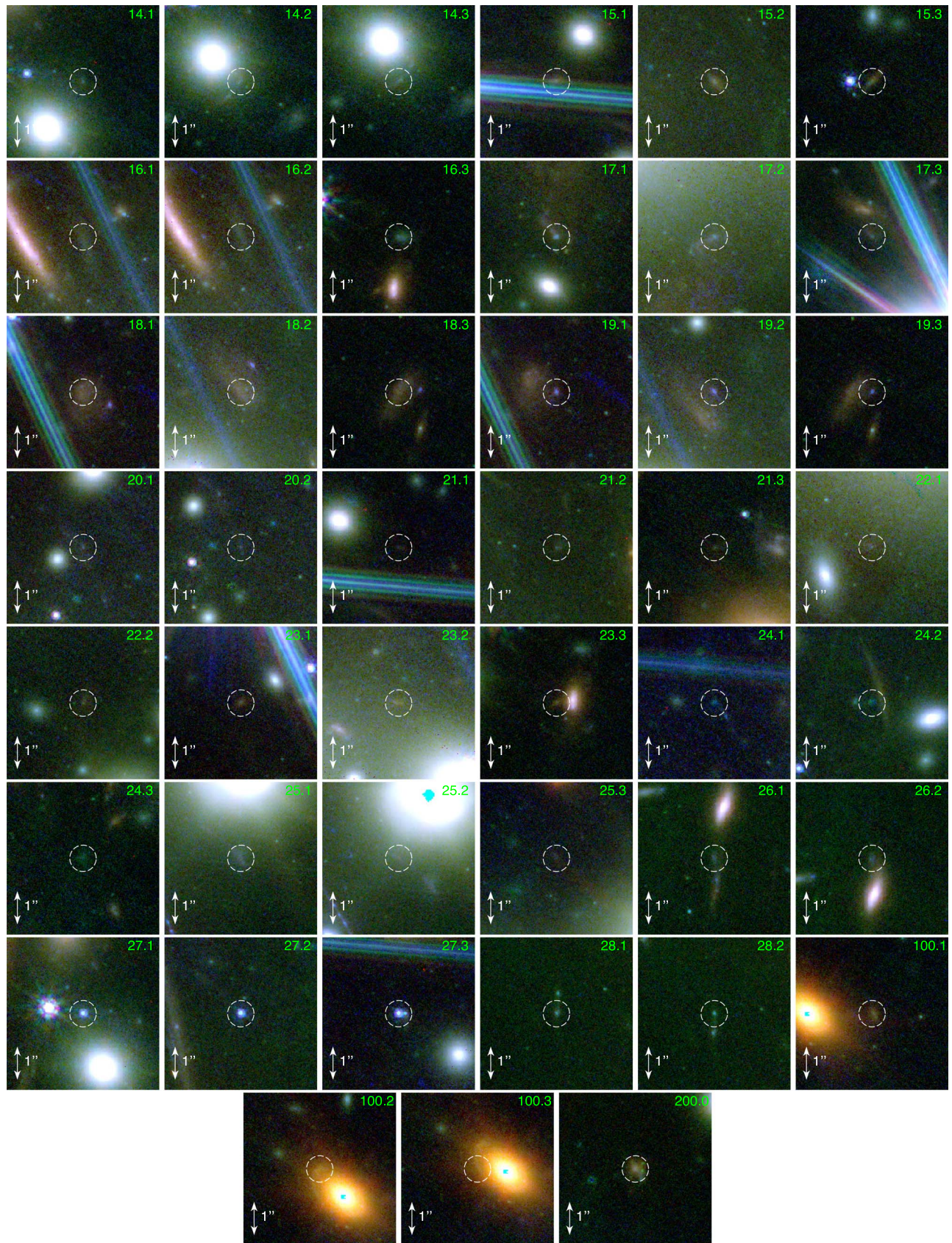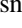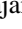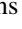
**Figure 14.** Continuing figure.

## ORCID iDs

Guillaume Mahler ⓘ https://orcid.org/0000-0003-3266-2001
Mathilde Jauzac ⓘ https://orcid.org/0000-0003-1974-8732
Johan Richard ⓘ https://orcid.org/0000-0001-5492-1049
Benjamin Beauchesne ⓘ https://orcid.org/0000-0002-0443-6018
Harald Ebeling ⓘ https://orcid.org/0000-0001-8249-2739
David Lagattuta ⓘ https://orcid.org/0000-0002-7633-2883
Priyamvada Natarajan ⓘ https://orcid.org/0000-0002-5554-8896
Keren Sharon ⓘ https://orcid.org/0000-0002-7559-0864
Hakim Atek ⓘ https://orcid.org/0000-0002-7570-0824
Adélaïde Claeyssens ⓘ https://orcid.org/0000-0001-7940-1816
Benjamin Clément ⓘ https://orcid.org/0000-0002-7966-3661
Dominique Eckert ⓘ https://orcid.org/0000-0001-7917-3892
Alastair Edge ⓘ https://orcid.org/0000-0002-3398-6916
Jean-Paul Kneib ⓘ https://orcid.org/0000-0002-4616-4989
Anna Niemiec ⓘ https://orcid.org/0000-0003-3791-2647

## References

Acebron, A., Jullo, E., Limousin, M., et al. 2017, MNRAS, 470, 1809
Asplund, M., Grevesse, N., Sauval, A. J., & Scott, P. 2009, ARA&A, 47, 481
Beers, T. C., Flynn, K., & Gebhardt, K. 1990, AJ, 100, 32
Bertin, E., & Arnouts, S. 1996, A&AS, 117, 393
Bradač, M., Schrabback, T., Erben, T., et al. 2008, ApJ, 681, 187
Buchner, J., Georgakakis, A., Nandra, K., et al. 2014, A&A, 564, A125
Caminha, G. B., Grillo, C., Rosati, P., et al. 2017, A&A, 600, A90
Caminha, G. B., Suyu, S. H., Mercurio, A., et al. 2022, A&A, 666, L9
Chang, C., Baxter, E., Jain, B., et al. 2018, ApJ, 864, 83
Claeyssens, A., Adamo, A., Richard, J., et al. 2023, MNRAS, 520, 2180
Coe, D., Salmon, B., Bradač, M., et al. 2019, ApJ, 884, 85
Collett, T. E., Buckley-Geer, E., Lin, H., et al. 2017, ApJ, 843, 148
Deason, A. J., Oman, K. A., Fattahi, A., et al. 2021, MNRAS, 500, 4181
Desprez, G., Richard, J., Jauzac, M., et al. 2018, MNRAS, 479, 2630
Diego, J. M., Broadhurst, T., Chen, C., et al. 2016a, MNRAS, 456, 356
Diego, J. M., Broadhurst, T., Wong, J., et al. 2016b, MNRAS, 459, 3447
Ebeling, H., Edge, A. C., & Henry, J. P. 2001, ApJ, 553, 668
Ebeling, H., Qi, J., & Richard, J. 2017, MNRAS, 471, 3305
Ebeling, H., White, D. A., & Rangarajan, F. V. N. 2006, MNRAS, 368, 65
Eckert, D., Finoguenov, A., Ghirardini, V., et al. 2020, OJAp, 3, 12
Elíasdóttir, Á., Limousin, M., Richard, J., et al. 2007, arXiv:0710.5636
Ettori, S., Baldi, A., Balestra, I., et al. 2015, A&A, 578, A46
Feroz, F., Hobson, M. P., Cameron, E., & Pettitt, A. N. 2019, OJAp, 2, 10
Fox, C., Mahler, G., Sharon, K., & Remolina González, J. D. 2022, ApJ, 928, 87
Freeman, P., Doe, S., & Siemiginowska, A. 2001, Proc. SPIE, 4477, 76
Fruscione, A., McDowell, J. C., Allen, G. E., et al. 2006, Proc. SPIE, 6270, 62701V
Ghosh, A., Williams, L. L. R., Liesenborgs, J., et al. 2021, MNRAS, 506, 6144
Gladders, M. D., & Yee, H. K. C. 2000, AJ, 120, 2148
Golubchik, M., Furtak, L. J., Meena, A. K., & Zitrin, A. 2022, ApJ, 938, 14
Gonzalez, A. H., George, T., Connor, T., et al. 2021, MNRAS, 507, 963
Grillo, C., Suyu, S. H., Rosati, P., et al. 2015, ApJ, 800, 38
Harvey, D., Robertson, A., Massey, R., & McCarthy, I. G. 2019, MNRAS, 488, 1572
Hoag, A., Huang, K. H., Treu, T., et al. 2016, ApJ, 831, 182
Jauzac, M., Clément, B., Limousin, M., et al. 2014, MNRAS, 443, 1549
Jauzac, M., Eckert, D., Schwinn, J., et al. 2016, MNRAS, 463, 3876
Jauzac, M., Mahler, G., Edge, A. C., et al. 2019, MNRAS, 483, 3082
Jauzac, M., Richard, J., Jullo, E., et al. 2015, MNRAS, 452, 1437
Johnson, T. L., & Sharon, K. 2016, ApJ, 832, 82
Jullo, E., Kneib, J.-P., Limousin, M., et al. 2007, NJPh, 9, 447
Jullo, E., Natarajan, P., Kneib, J.-P., et al. 2010, Sci, 329, 924
Kneib, J.-P., Ellis, R. S., Smail, I., Couch, W. J., & Sharples, R. M. 1996, ApJ, 471, 643
Kneib, J.-P., & Natarajan, P. 2011, A&ARv, 19, 47
Lagattuta, D. J., Richard, J., Bauer, F. E., et al. 2019, MNRAS, 485, 3738
Lagattuta, D. J., Richard, J., Bauer, F. E., et al. 2022, MNRAS, 514, 497
Lam, D., Broadhurst, T., Diego, J. M., et al. 2014, ApJ, 797, 98
Lam, M. T., Ellis, J. A., Grillo, G., et al. 2018, ApJ, 861, 132
Limousin, M., Richard, J., Jullo, E., et al. 2007, ApJ, 668, 643
Lotz, J. M., Koekemoer, A., Coe, D., et al. 2017, ApJ, 837, 97
Mahler, G., Richard, J., Clément, B., et al. 2018, MNRAS, 473, 663
Mahler, G., Sharon, K., Fox, C., et al. 2019, ApJ, 873, 96
Markevitch, M., Gonzalez, A. H., Clowe, D., et al. 2004, ApJ, 606, 819
Montes, M. 2019, arXiv:1912.01616
Montes, M., & Trujillo, I. 2014, ApJ, 794, 137
Montes, M., & Trujillo, I. 2022a, ApJL, 940, L51
Montes, M., & Trujillo, I. 2022b, ApJL, 940, L51
Mowla, L., Iyer, K. G., Desprez, G., et al. 2022, ApJL, 937, L35
Natarajan, P., & Kneib, J.-P. 1997, MNRAS, 287, 833
Newman, A. B., Treu, T., Ellis, R. S., & Sand, D. J. 2013a, ApJ, 765, 25
Newman, A. B., Treu, T., Ellis, R. S., et al. 2013b, ApJ, 765, 24
Pascale, M., Frye, B. L., Diego, J., et al. 2022, ApJL, 938, L6
Randall, S. W., Markevitch, M., Clowe, D., Gonzalez, A. H., & Bradač, M. 2008, ApJ, 679, 1173
Repp, A., & Ebeling, H. 2018, MNRAS, 479, 844
Richard, J., Claeyssens, A., Lagattuta, D., et al. 2021, A&A, 646, A83
Richard, J., Kneib, J.-P., Ebeling, H., et al. 2011, MNRAS, 414, L31
Schwarz, G. 1978, AnSta, 6, 461
Schwinn, J., Jauzac, M., Baugh, C. M., et al. 2017, MNRAS, 467, 2913
Sharon, K., Bayliss, M. B., Dahle, H., et al. 2020, ApJS, 247, 12
Sharon, K., Chen, M. C., Mahler, G., Coe, D. & the RELICS Collaboration 2023, ApJS, 264, 15
Sharon, K., Gladders, M. D., Marrone, D. P., et al. 2015, ApJ, 814, 21
Sharon, K., & Johnson, T. L. 2015, ApJL, 800, L26
Smith, G. P., Kneib, J.-P., Smail, I., et al. 2005, MNRAS, 359, 417
Soucail, G., Fort, B., Mellier, Y., & Picat, J. P. 1987, A&A, 172, L14
Umetsu, K., Birkinshaw, M., Liu, G.-C., et al. 2009, ApJ, 694, 1643
Vanzella, E., Caminha, G. B., Rosati, P., et al. 2021, A&A, 646, A57
Verdugo, T., Motta, V., Muñoz, R. P., et al. 2011, A&A, 527, A124
Voges, W., Aschenbach, B., Boller, T., et al. 1999, A&A, 349, 389
Wang, X., Hoag, A., Huang, K.-H., et al. 2015, ApJ, 811, 29
Weilbacher, P. M., Palsa, R., Streicher, O., et al. 2020, A&A, 641, A28
Willingale, R., Starling, R. L. C., Beardmore, A. P., Tanvir, N. R., & O'Brien, P. T. 2013, MNRAS, 431, 394
Wittman, D., Golovich, N., & Dawson, W. A. 2018, ApJ, 869, 104
Wong, K. C., Ammons, S. M., Keeton, C. R., & Zabludoff, A. I. 2012, ApJ, 752, 104
Zitrin, A., Fabris, A., Merten, J., et al. 2015, ApJ, 801, 44